

Development of a cost-effective X-ray imaging device based on Raspberry Pi Camera

Nguyen Duc Ton^{a,f}, Nguyen Thanh Luan^{b,g}, Faizan Anjum^a, D. Joseph Daniel^b, Sunghwan Kim^c, Suchart Kothan^d, Jakrapong Kaewkhao^e and Hong Joo Kim^{a,b*}

^a Department of Physics, Kyungpook National University, Daegu, 41566, South Korea

^b Center of High Energy Physics, Kyungpook National University, Daegu, 41566, South Korea

^c Department of Radiological Science, Cheongju University, Cheongju, 28503, Korea

^d Center of Radiation Research and Medical Imaging, Department of Radiologic Technology, Faculty of Associated Medical Sciences, Chiang Mai University, Chiang Mai, 50200, Thailand

^e Center of Excellence in Glass Technology and Materials Science, Nakhon Pathom Rajabhat University, Nakhon Pathom, 73000, Thailand

^f Institute for Nuclear Science and Technology, Vietnam Atomic Energy Institute, Hanoi, 11307, Vietnam

^g Institute of Physics, Vietnam Academic of Science and Technology, Hanoi, 11307, Vietnam

E-mail: hongjoo@knu.ac.kr

ABSTRACT: This study reports the development and characterization of a cost-effective X-ray imaging device built from Raspberry Pi components, including a high-quality 12.3-megapixel camera configured for indirect detection with a Gd₂O₂S: Tb scintillation screen. The device was evaluated under both ambient light and X-ray exposure conditions. Initial characterization under ambient light ensured proper optical focusing; subsequently, camera settings (ISO and exposure time) were evaluated and optimized for X-ray imaging performance. Spatial resolution of the developed device was quantified using the Slanted-Edge method to derive the Modulation Transfer Function (MTF). The device achieves MTF₂₀ values of 68 lp/mm under ambient light and 25 lp/mm under X-ray irradiation (50 and 70 kV) with Gd₂O₂S:Tb screen. Besides, the modularity of the developed device was confirmed by conducting the tests with LYSO:Ce and GAGG:Ce screens. Results demonstrate that this compact, cost-effective platform delivers spatial resolution comparable to clinical radiography systems, with potential applications in scientific, educational, and medical contexts where cost and portability are critical factors.

KEYWORDS: Raspberry Pi; digital radiography, X-ray; spatial resolution; indirect conversion.

1. Introduction

X-ray imaging is one of the most transformative techniques in non-destructive testing, providing non-invasive access to the internal structure of objects and biological tissues. Since the first discovery in the 1890s, it has long served as a versatile tool across diverse fields, from industry, security to scientific research, and medicine due to its exceptional penetration capability [1–5]. In industry and security applications, X-ray imaging provides powerful means of non-destructive testing for quality control and safety, allowing internal inspection of complex assemblies such as welds, electronic circuits and composite materials without damaging the object. In airport and cargo security, X-ray scanners help to detect concealed items such as metals, plastics, explosives, and electronics through color-coded images [6–13]. They improve screening efficiency, meet international security standards, and allow real-time inspection of passenger

luggage and cargo. For large-scale freight, X-ray imaging systems range from small cabinet scanners to drive-through units for vehicles and containers, incorporating automated detection, material identification, and AI-based image analysis for faster and more reliable screening [10, 12, 14–17]. In healthcare, it enables non-invasive visualization of internal body structures for diagnosing fractures, bone diseases, pulmonary disorders, and foreign objects, while advanced modalities such as computed tomography and mammography further enhance diagnostic precision [5, 18–21]. Besides these practical applications, X-ray imaging also plays a crucial role in scientific research, including crystallography, synchrotron diagnostics, and radiation monitoring. Ongoing advances in detector design, scintillation materials, and computational imaging continue to enhance its resolution, sensitivity, and versatility, broadening its impact across multiple scientific and technological fields [22–33].

Screen film radiography, once dominant, was limited by its narrow dynamic range, chemical processing challenges, and storage difficulties [34–41]. Its replacement by digital radiography brought extended dynamic range, dose efficiency, advanced image processing, and seamless integration with Picture Archiving and Communication Systems [25, 26, 40]. Two main technologies underpin this shift: Computed Radiography (CR), using cassette-based storage-phosphor plates [30, 34, 36, 42–44], and Direct Digital Radiography (DR), employing flat-panel detectors for immediate acquisition [30, 45–52]. Digital radiography employs either indirect conversion, where scintillators such as CsI(Tl) or Gd₂O₂S:Tb (GOS) convert X-rays into light before photodetection, efficient but leading to light scatter [26, 33, 53, 54], or direct conversion, typically with amorphous selenium (α -Se), which converts X-rays directly to charge for higher spatial resolution [30, 44, 49, 54–56]. Indirect systems dominate general imaging for dose efficiency, while direct systems are preferred for high-resolution applications [24, 54, 57–59]. Despite advances, current systems remain costly, bulky, and inaccessible for small-scale research, education, and resource-limited settings. Achieving low-dose, high-resolution, and large-area coverage in a compact, affordable form remains a challenge [22, 26, 60–62].

Recent progress in compact electronics and open-hardware platforms offers a solution [63–67]. The Raspberry Pi, a low-cost computer with strong community support, enables modular, portable systems [68–73]. In addition, the Sony IMX477 CMOS sensor integrated into the Raspberry Pi High Quality (RPi HQ) camera adopts a back-illuminated architecture. This design reduces optical losses, thereby enhancing photon collection efficiency. Thus, the sensor demonstrates improved quantum efficiency, sensitivity, and a higher signal-to-noise ratio, rendering it well suited for high-efficiency, low-noise imaging applications while preserving cost-effectiveness [74, 75]. Building on these capabilities, an imaging device was designed for affordability, portability, and ease of use, employing commercially available components to ensure broad accessibility across applications. Its streamlined data-processing workflow, implemented through straightforward algorithms that analyze light intensity from the integrated camera, enables efficient acquisition and interpretation of imaging data, enhancing usability in diverse operational contexts. This work presents a Raspberry Pi-based digital X-ray imaging system in indirect configuration, utilizing a lens-coupled camera, a prism/reflector mirror, and a GOS scintillation screen. The performance evaluation began with a systematic analysis of key imaging metrics, including readout noise, modulation transfer function (MTF), signal-to-noise ratio (SNR), and contrast under varying X-ray conditions, as well as the effects of camera settings such as ISO and exposure time. These findings underscore the feasibility of developing a high-

quality, affordable, and portable radiography system for broad use in education, research, and real-world applications.

2. Instrument configuration and measurement method

2.1 Instrument configuration

The system was designed by following the indirect detection concept, which converts attenuated X-rays into visible light via a GOS scintillation screen. The experimental setup is shown in Fig. 1. A lens-prism optical assembly redirects and focuses the light onto the RPi HQ camera, with a $15\times 15\times 15$ mm prism deflecting the optical path to protect radiation-sensitive electronics. The indirect imaging process begins when transmitted X-rays, carrying the object's attenuation-dependent intensity pattern, interact with the GOS scintillator screen. The scintillator absorbs the attenuated X-rays and converts their deposited energy into visible light through luminescence, thereby forming a two-dimensional optical image. The emitted light is guided through the optical prism, which deflects it by 90° toward the imaging lens. The “folded” optical path is a key design feature that relocates the radiation-sensitive camera sensor away from the primary X-ray beam, effectively preventing radiation-induced degradation and reducing image noise. Following redirection, an optical lens system collects the redirected photons, focusing them on the Raspberry Pi high-quality camera. The Raspberry Pi computer subsequently controls the camera's acquisition parameters and captures the resulting digital image for storage and further processing.

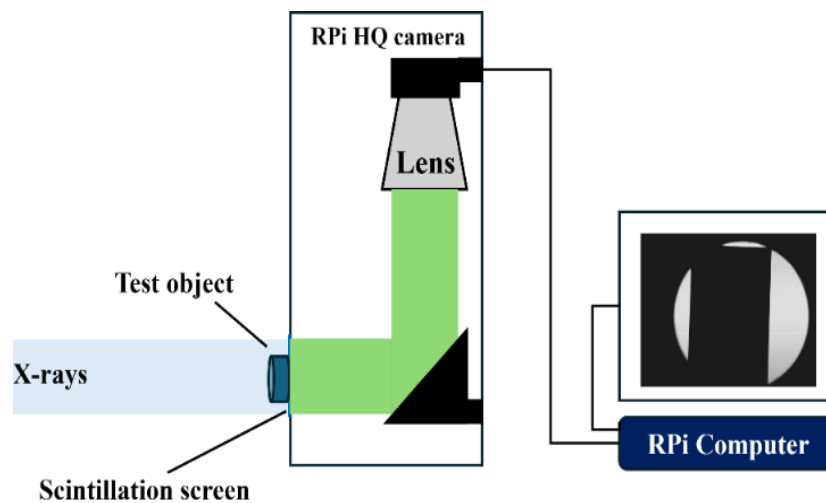


Figure 1. Schematic layout of the developed X-ray imaging device in indirect conversion configuration with lens-prism coupled.

The device's central hardware consists of a Raspberry Pi 4 Model B computer paired with its high-quality camera module. While the camera serves as a photosensor, image acquisition and processing are fully controlled by the Raspberry Pi 4B computer, which features onboard storage, multiple connectivity options, and an HDMI output [68, 69]. The imaging sensor is a camera based on a Sony IMX477 sensor, featuring a resolution of 12.3 MP (4056×3040) and a $1.5\ \mu\text{m}$ pixel pitch. With the advantages of CMOS technology, the RPi HQ camera offers relatively low noise, high readout speed, and lower power consumption at a reduced cost. The electronic read noise of RPi HQ camera has been reported to be approximately $3\ e^-$ rms per pixel, placing the

Sony IMX477 in the regime of scientific-grade CMOS sensors and enabling low-noise imaging at relatively low signal levels [75]. Moreover, the back-illuminated architecture of the Sony IMX477 sensor relocates the metal interconnects and transistor layers to the rear side of the photodiode, removing these structures from the optical path. This configuration increases the effective fill factor and photon collection efficiency, thereby enhancing quantum efficiency, improving low-light sensitivity, and reducing readout and shot-noise contributions compared with conventional front-illuminated designs [64, 65, 69, 74, 75]. For the indirect imaging setup, it was fitted with a 16 mm CS-mount lens, aligned to an optical prism. Tab. 1 presents detailed information about the RPi HQ camera, which was built on Sony IMX477.

Table 1. Basis information of Raspberry Pi High-Quality camera [69, 74, 75].

Architect	Back-illuminated and staked CMOS image sensor
Maximum frame rate	40 (12 bit-images)
Image size	Diagonal 7.857 mm (Type 1/2.3)
Number of active pixels	4056 (H) × 3040 (V)
Chip size	7.564 mm (H) × 5.476 mm (V)
Pixel size	1.55 μm (H) × 1.55 μm (V)
Read noise	3 e ⁻ (rms)

The camera’s interchangeable C/CS mount compatibility and back focusing mechanism allow precise lens-to-sensor adjustment, ensuring sharp focus and adaptability for diverse scientific imaging applications. The sensitivity spectra of the RPi HQ camera based on the Sony IMX477 sensor, as presented in Fig. 2, indicates that the RPi HQ camera achieves peak sensitivity in the 400 - 700 nm range, making it well-suited for indirect detection, where incoming X-rays are converted to visible photons by scintillation screens. Accordingly, a thin GOS screen, characterized by emissions between 450-700 nm, was selected for initial evaluations. The X-ray induced luminescence spectrum of GOS was measured and is presented in Fig. 3.

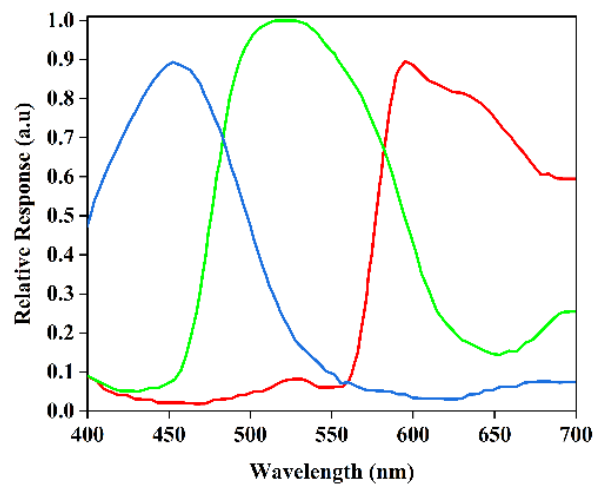


Figure 2. Sensitivity spectra of the RPi HQ camera based on Sony IMX477. Data was extracted from [69].

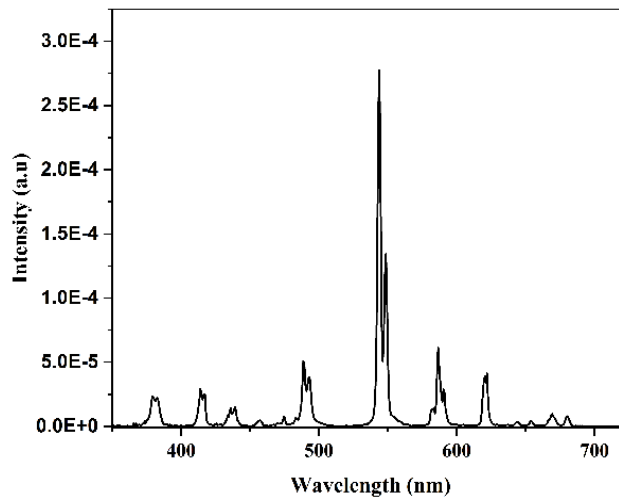


Figure 3. Emission spectrum of $\text{Gd}_2\text{O}_2\text{S}:\text{Tb}$ screen under X-ray excitation.

The Raspberry Pi 4B computer plays the role of the central control and data acquisition unit. The system operates at nominal power consumption of 12–15 W under typical image processing loads, significantly lower than conventional desktop or server-grade systems, enabling integration into compact laboratory setups with minimal thermal management requirements. Remote operation is facilitated through three complementary protocols: (1) SSH for secure command-line access and automated script execution, enabling headless operation and batch processing; (2) VNC for remote graphical desktop access, suitable for real-time image monitoring and parameter adjustment; and (3) Raspberry Pi Connect, a proprietary cloud-based remote desktop service providing intuitive browser-based access without complex configuration. All protocols operate over standard Ethernet or LAN connectivity, accessible from local laboratory networks or external locations via secure connection. From a radiation safety perspective, remote operation implements the ALARA (As Low As Reasonably Achievable) principle's "distance" strategy: by permitting fully control from a separated location, operator proximity to the radiation source is minimized, and cumulative exposure duration is reduced compared to on-site operation. This engineering control measure is particularly valuable for occupational dose minimization in research facilities where imaging system utilization spans extended periods or involves multiple operators, ensuring compliance with regulatory dose limits while maintaining measurement efficiency. For data handling, the system utilizes an SD card for storage and provides multiple connectivity options for straightforward data transmission. A custom Python-based program, built upon standard Raspberry Pi camera libraries and documents, was developed to manage all camera operations and dynamically adjust settings, including exposure mode, ISO, and exposure time [69, 74, 75].

To achieve the sharp and clear images within a compact imaging system, the optical imaging system was built around a RPi HQ camera and its official 16 mm, 10 MP C-mount lens. The optical path was designed for compactness, featuring a total air-gap distance of approximately 60 mm (from the scintillator to the prism and from the prism to the lens), and a 15 mm thick optical prism. This configuration resulted in an effective object distance that was considerably shorter than the lens's specified Minimum Object Distance (MOD) of 200 mm. A lens could not resolve an image from an object closer than its MOD when set to the standard 17.53 mm C-mount flange

distance. Therefore, the back-focus adjustment ring, an integrated feature of the RPi HQ camera, was essential to the design. We utilized this mechanism to carefully adjust the lens-to-sensor distance, thereby compensating for the unusually short object distance and achieving a sharp focus on the scintillation screen. For final assembly, the lens's aperture and primary focusing ring were then finely adjusted to achieve the sharpest possible image. Although not inherently designed for low-light applications, the RPi HQ camera achieved effective performance in this setup by operating at a low f-number to enhance light throughput. To reduce ambient noise and shield sensitive components from radiation exposure, the camera sensor, lens, and prism were enclosed in an aluminum housing, as presented in Fig. 4. During experiments, the scintillation screen was attached to the optical window on the cover frame.

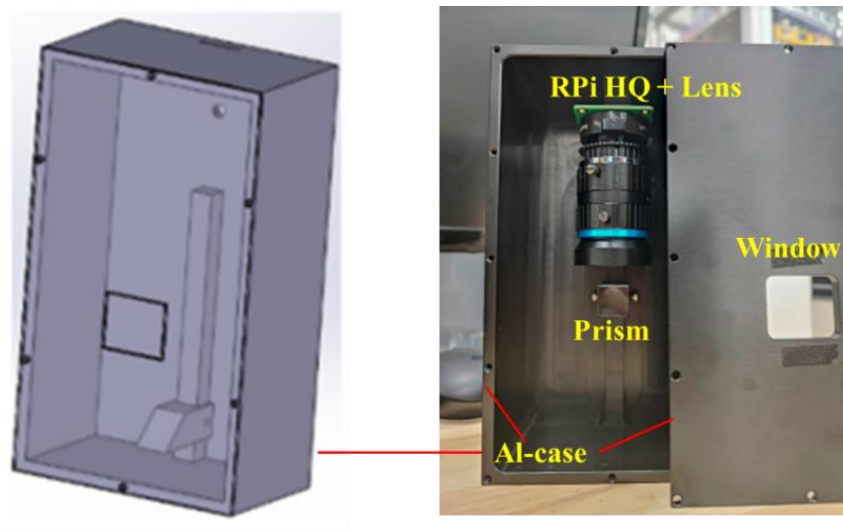


Figure 4. (Left) Mechanical drawing of the Aluminum case and (right) the photograph of the optical component installed inside the case.

As the primary design objective of this platform is accessibility through cost-effectiveness, the system was developed using readily available components rather than specialized instrumentation or custom-fabricated parts. It leverages the mature Raspberry Pi ecosystem and standard optical and mechanical elements sourced from high-volume commercial suppliers. This design philosophy promotes wide adoption across educational, research, and resource-limited applications. The total cost of the imaging platform, excluding the X-ray source (typically \$5000-\$50000, available in radiography facilities), depending on type and quality of scintillation screen was estimated around \$570. Furthermore, owing to its indirect conversion configuration, the device offers inherent versatility and can be adapted for imaging with other excitation sources, such as neutron or proton beams, by selecting appropriate scintillation materials and optimizing camera parameters.

2.2 Measurement method

After fabrication, the system's performance was evaluated at room temperature. The low-noise characteristics of the RPi HQ camera were verified by capturing 10 dark frames at various ISO and exposure settings with the optical window closed, then calculating the standard deviation. The effects of ISO (100-800) and exposure time (100-2000 ms) on image contrast were assessed at a constant X-ray tube voltage of 70 kV. All images were saved as 12-bit PNG files, in gray

scale at the sensor's maximum resolution (4056×3040). Contrast level in percentage was calculated from fixed-size regions of interest (ROIs) in bright and dark regions using:

$$C = \frac{I_{max} - I_{min}}{I_{max} + I_{min}} \times 100\%$$

where I_{max} and I_{min} are pixel intensity in bright and dark areas, respectively. The ROI selection is illustrated in Fig. 5. ROIs were selected as uniform 200×200 pixel areas to minimize artifacts and ensure consistent measurements. This standardized approach was maintained across all measurements for reproducibility.

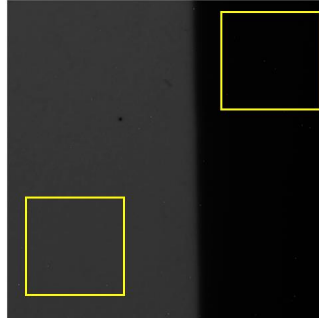


Figure 5. An example of ROIs selection for contrast calculation. Two regions were selected on the bright and dark sides to determine the bright and dark levels.

Once the optimal camera settings were determined, the device was then installed for imaging with a standard hospital X-ray head, as shown in Fig. 6, with the source-to-screen distance fixed at 40 cm while the collimators were adjusted to focus X-ray beam to scintillation screen. Images were acquired at various tube voltages (kV), currents (mA), and durations (ms), as listed in Table 2.

Table 2. Parameters of X-ray beam (kV-mA-ms) at various exposure conditions (kV-mAs) for MTF evaluation.

mAs/kV	50 kV	70 kV
5	100 mA-50 ms	100 mA-50 ms
10	100 mA-10 ms	100 mA-10 ms
15	100 mA-150 ms	100 mA-150 ms
20	100 mA-200 ms	100 mA-200 ms
30	200 mA-150 ms	200 mA-150 ms
40	200 mA-200 ms	200 mA-200 ms

For the preliminary evaluation, the device's performance was assessed using MTF, image contrast, and SNR as a function of exposure dose (mAs or R) at tube voltages of 50 and 70 kV. SNR was computed from a uniform bright ROI by:

$$SNR = \mu / \sigma$$

Where μ and σ are the mean pixel intensity and the standard deviation of the selected ROI, respectively. The consistent size and location across images were optimized to reduce statistical uncertainty and ensure consistency among images. Due to instrumentation limitations, X-ray fluence was not measured; consequently, further performance parameters, including Detective

Quantum Efficiency (DQE) and Normalized Noise Power Spectrum (NNPS) per IEC 62220-1 standards, would not be accessed [75–79].

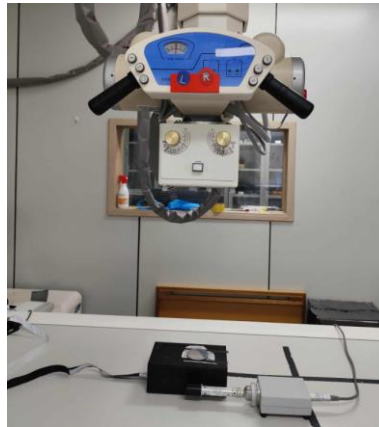


Figure 6. Experimental setup with a clinical X-ray source; source-to-screen distance 40 cm. A RadCal Mod 10X5-6 dosimeter measured exposure dose at the scintillator surface.

Principally, the resolving power of an imaging system, expressed as MTF, could be derived by measuring different spread functions, as illustrated in Fig. 7. The slanted-edge method was employed to evaluate the system’s Modulation Transfer Function (MTF). This method is recognized for its high precision, effective noise reduction through averaging, and strong compatibility with digital image processing, making it well-suited for assessing the spatial resolution of digital imaging systems [76–80]. An illustration of the slanted-edge method is shown in Fig. 8.

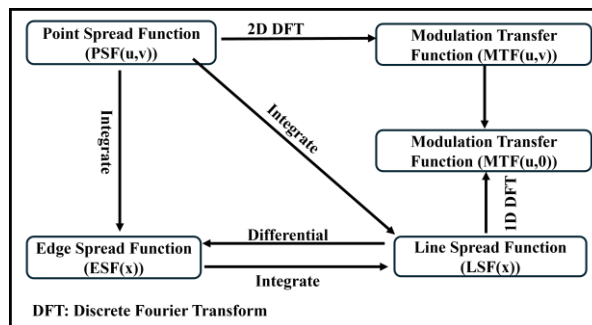


Figure 7. Illustration of the relation between the spread functions and the MTF calculations.

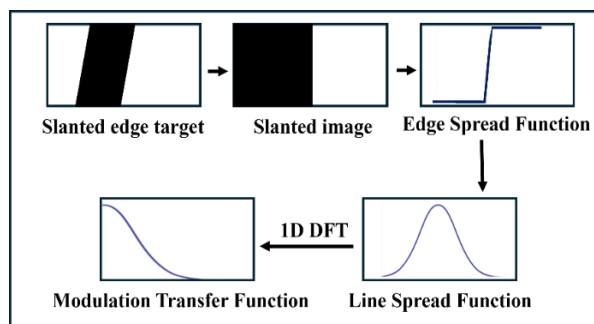


Figure 8. Schematic diagram of the Slanted Edge method that was used for MTF measurement.

Edge images of the test object were acquired at the camera’s maximum resolution and saved into 12-bit PNG files. The method analyzes the system’s response to a high-contrast edge positioned at a slight angle to the pixel grid. Following the recommendations from the International Electrotechnical Commission (IEC) to evaluate the performance of X-ray imaging devices, a homemade W plate with 0.1 mm of thickness and a sharp, well-polished edge was attached to the GOS screen at a 2–5° tilted [79, 81, 82]. From the edge images, the Edge Spread Function (ESF) was derived, differentiated to obtain the Line Spread Function (LSF), and Fourier-transformed to yield the MTF [83, 84]:

$$LSF(x) = \frac{d}{dx}ESF(x)$$

$$MTF(u, 0) = |F[LSF(x)]|$$

To validate the MTF extraction, a Teledyne Remote RadEye HR sensor with Min-R (Gd₂O₂S: Tb) scintillation film was used [85, 86]. For this setup, the prepared W target was mounted on the sensor’s protective layer to acquire X-ray images, from which the MTF curve was extracted and compared with Teledyne’s reference data [87]. The recorded X-ray image and corresponding MTF curve are presented in Fig. 9. The measured MTF exceeds the reference Min-R data at low spatial frequencies, indicating improved performance in that range, but falls off more rapidly beyond the spatial frequency value of approximately 6 lp/mm, reflecting a reduction in high-frequency response. These differences likely stem from variations in experiment conditions and data processing. Overall, the results agree reasonably well with reference data, confirming the reliability of the MTF evaluation. However, the lens-prism coupling inherently reduces the photon throughput, lowering quantum efficiency and SNR as noted in previous studies [21, 88–90]. It should be noted that except read noise measurements, dark-frame correction has been systematically implemented to account for these variations, thereby improving measurement accuracy and uniformity across the sensor during data analysis.

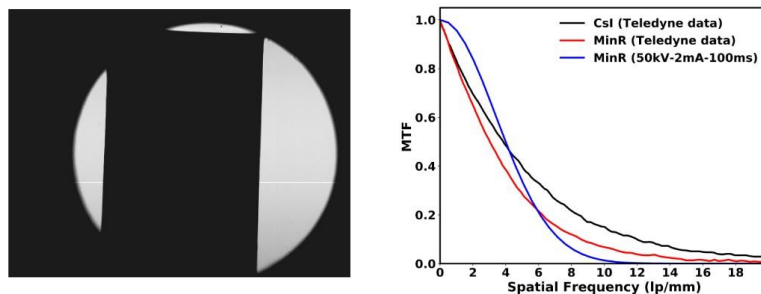


Figure 9. (Left) X-ray image recorded by RadEye Remote HR sensor and (right) extracted MTF curve from the captured images (blue line) in compared with its published data (black and red).

3. Results and discussion

3.1 Optical performance verification

After assembly, the device’s optical alignment and resolution were verified by replacing the scintillation screen with a standard optical resolution target for ambient-light testing. As shown in Fig. 10, bar patterns up to approximately 30-40 lp/mm were clearly resolved, confirming accurate focusing and optical performance. Based on the slanted-edge method, the MTF curves

(Fig. 11) under ambient light yielded approximately 68 lp/mm at 20% of MTF (MTF_{20}), demonstrating high spatial resolution and establishing a strong baseline before X-ray imaging.

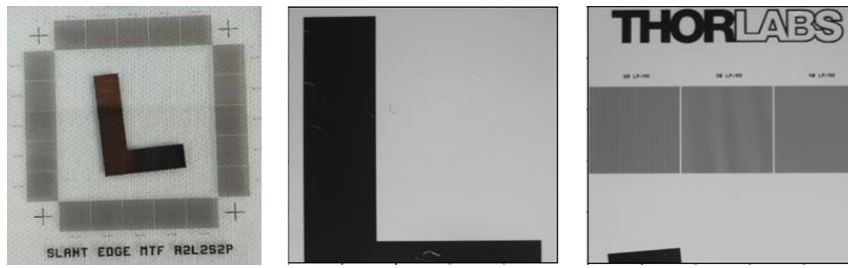


Figure 10. The standard resolution target THORLAB R2L2S2P and its optical images were captured by the developed device.

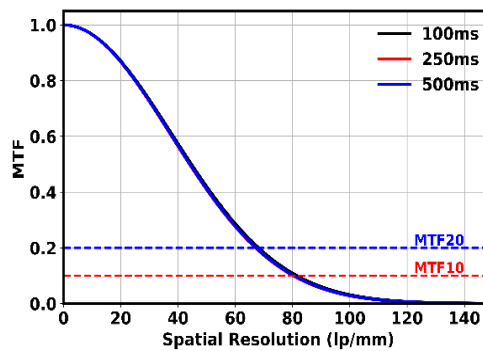


Figure 11. MTF curves of the developed device under test at ISO100, various exposure times.

3.2 Read noise characterization

The read noise or dark noise of the RPi HQ camera was evaluated across ISO (100-800) and exposure times by capturing and averaging five dark frames, then extracting histograms, mean values, and standard deviations.

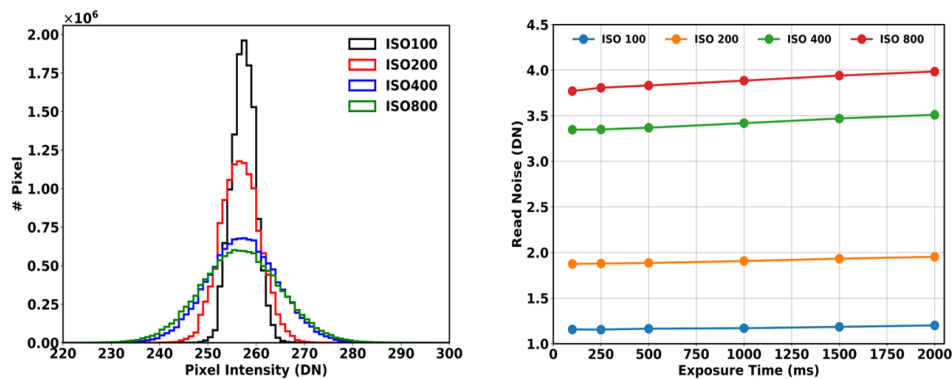


Figure 12. (a) Illustration of image histogram of dark image for readout noise evaluation at different ISO settings, 250 ms of exposure time, and (b) measured readout noise (DN) at different ISO settings, exposure times.

As shown in Fig. 12(a), higher ISO broadened and flattened the histograms, indicating increased noise from amplified signal and noise components while the mean values stabilized at 256-257.5. This trend is indicative of increased noise, primarily due to the amplification of both signal and noise components at higher ISO settings. ISO 100 exhibits the narrowest distribution,

confirming its superior noise performance. Fig. 12(b) shows that the read noise (standard deviation) increases slightly with longer exposures, particularly at high ISO, suggesting a minor temporal noise component from dark current or thermal effects. ISO gain remained the dominant noise source, with ISO 800 being the highest and ISO 100 being the lowest.

Overall, the RPi HQ camera, which is based on a CMOS sensor, exhibits low intrinsic noise at low ISO settings and stable performance across various exposure times [64, 65, 91]. Even at the highest ISO setting (800) and a long exposure time (2000 ms), the standard deviation is approximately 4, corresponding to less than 1.6 % deviation relative to the mean value of the recorded images. This further demonstrates the low-noise performance of the Raspberry Pi HQ camera. These characteristics are essential for high-fidelity and low-noise imaging, underscoring the suitability of the developed device for precision imaging applications such as X-ray and scientific imaging, where noise performance is critical. Following ambient-light verification, the system was tested in X-ray configuration at 70 kV - 2 mA, with a 3 cm distance between the source and the object. Fig. 13 shows captured images, demonstrating the device's capability for X-ray imaging and its potential for non-destructive testing and inspection. Based on this, further evaluations, optimizations are planned, which will be discussed later.

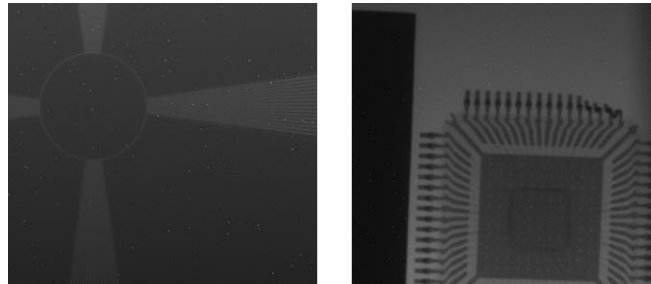


Figure 13. Recorded images of (left) Pb star test pattern and (right) the W-plate alongside an electronic microchip under X-ray irradiation.

3.3 Effect of ISO and exposure time settings

As mentioned previously, although the RPi HQ camera is not designed for low-light use, its performance can be improved through optical adjustments (back-focus alignment, low f-number) and careful optimization of ISO and exposure time. ISO acts as a gain control, increasing brightness but also amplifying noise. In contrast, longer exposures collect more photons but also increase the readout noise, which could be measured from dark frames. A trade-off between sensitivity and noise makes systematic testing essential. To investigate this, slanted-edge images of the W-target under X-ray irradiation were recorded at various ISO and exposure settings, then their corresponding histograms, contrast values were extracted. The images obtained at various ISO-exposure time settings are displayed on Fig. 14. As clearly shown, higher ISO and longer exposure both increase brightness, confirming that a greater dose yields a stronger scintillation signal. Contrast curves measured from fixed ROIs with various exposure times and ISO are plotted in Fig. 15. Contrast rose gradually with exposure to low ISO but reached a plateau beyond 500 ms at higher ISOs. ISO 400 at 500 ms provided approximately 73% contrast with efficient exposure and manageable noise, making it well-balanced for dose-limited or dynamic X-ray imaging. With these optimized settings, the device was further evaluated using a standard hospital X-ray machine, varying tube current and exposure time to study their effects on contrast, SNR and MTF.

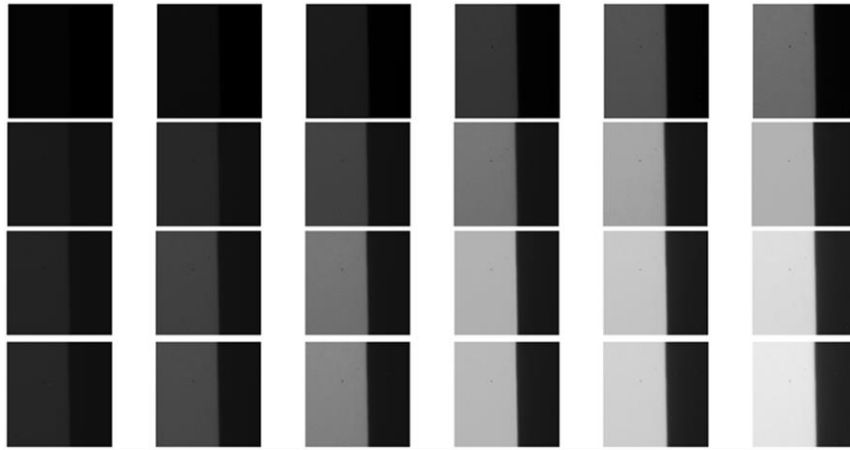


Figure 14. Slanted images recorded under X-ray irradiation with various ISO-exposure time settings: from top to bottom: ISO100, 200, 400 and 800, from left to right: exposure time from 100 – 2000 ms.

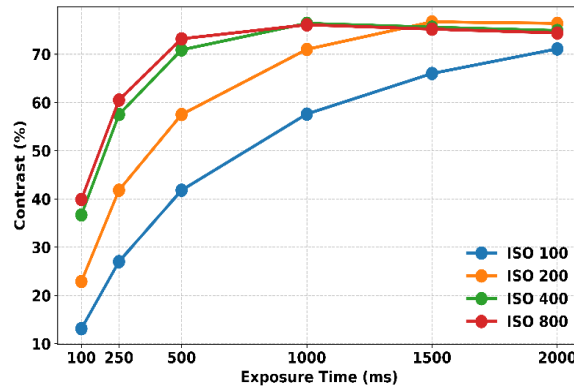


Figure 15. The relationship between image contrast and ISO-exposure times of recorded images under 70 kV-2 mA X-ray.

3.4 Modulation Transfer Function

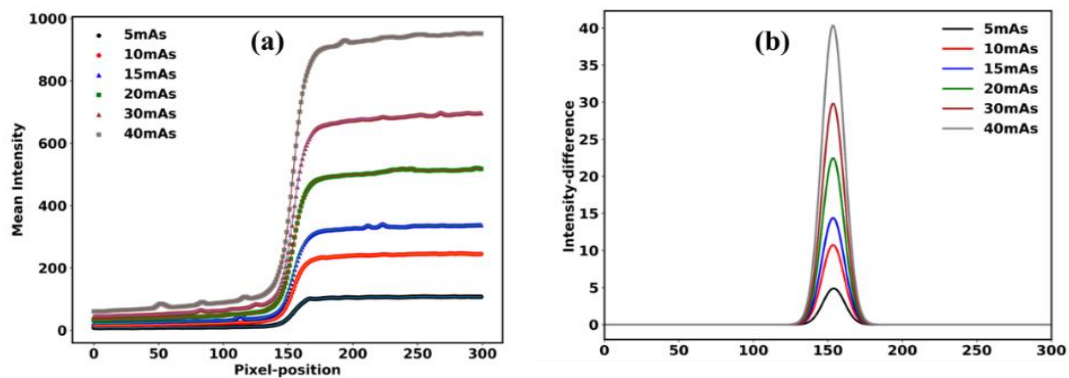


Figure 16. (a) The extracted Edge Spread Function and (b) corresponding Line Spread Function of the W-plate object under X-ray irradiation of 50 kV with different mAs values.

To quantify spatial resolution, slanted-edge images of the W target under 50 kV X-ray exposure were processed to extract the ESF and LSF, as shown in Fig. 16. The analysis

incorporated the camera's 1.55 μm pixel size during Fourier transformation, enabling accurate MTF curves across a wide spatial frequency range. These results establish a baseline for evaluating system performance under varying X-ray conditions. Figs. 17 and 18 illustrate the strong dependence of spatial resolution on both X-ray tube voltage (kV) and exposure level (mAs) in the indirect imaging system using a GOS scintillator. At 50 kV tube voltage, the X-ray beam has limited penetration depth and a higher absorption cross-section, causing most photons to be absorbed near the entrance surface of the scintillator [92, 93]. This shallow interaction leads to increased light scatter within the phosphor layer, degrading the MTF and reducing image sharpness. As the voltage increases (70 kV), the more energetic photons penetrate deeper into the scintillator, interacting closer to the camera sensor. This shift reduces the optical path length and internal scattering, resulting in a more confined light distribution and improved spatial resolution. This interpretation is supported by the results of MTF at 70 kV: the MTF values at high spatial frequency are slightly enhanced by increasing mAs. To clarify this energy-dependent relationship, we analyzed the X-ray spectra and quantified the mAs-to-exposure-dose correlation across the kilovoltage range (50 and 70 kV). Fig. 18 presents the simulated X-ray spectra for each tested voltage and the resulting exposure dose as a function of exposure level (mAs). These spectral and dosimetric analyses reveal that spatial resolution is jointly affected by tube voltage, which controls photon penetration and energy deposition, and by exposure level, which governs dose, thereby affecting signal strength. Effective imaging thus requires careful co-optimization of voltage and exposure parameters to maximize resolution within acceptable dose constraints.

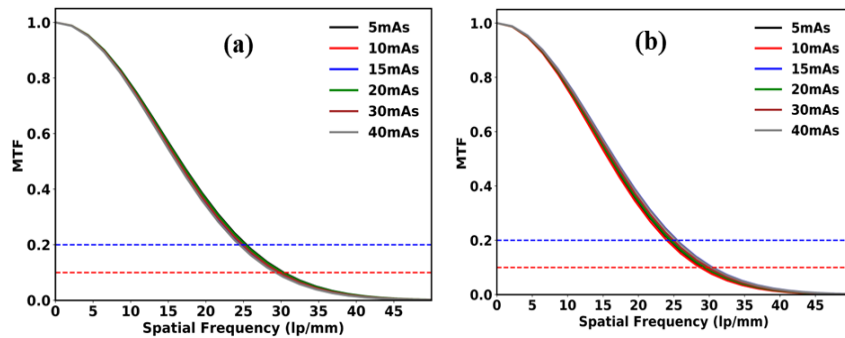


Figure 17. The extracted MTF curves from edge images under X-ray irradiation at (a) 50 kV and (b) 70 kV with various mAs values.

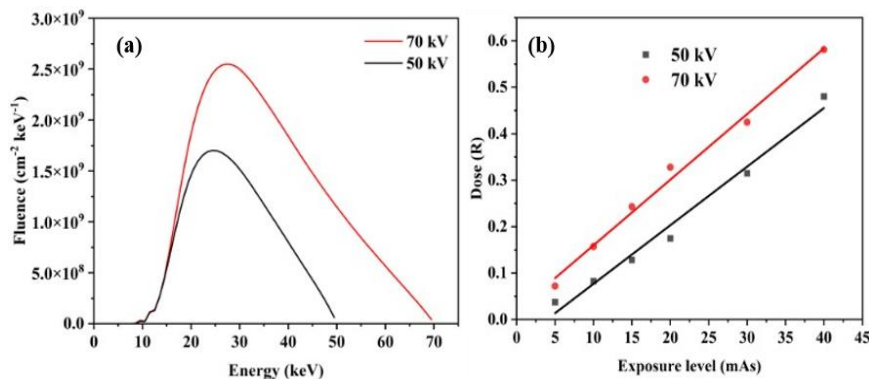


Figure 18. (a) Simulated energy spectrum of X-ray at various tube voltages (kV), 40 mAs by using SpekPy toolkit [94, 95] and (b), measured dose at various kV-mAs settings.

3.5 Image Contrast and Signal-to-Noise Ratio

Besides the MTF analysis, image contrast and signal-to-noise ratio (SNR) are strongly influenced by the X-ray tube voltage, as shown in Figs.19 and 20. The observed inverse relationship between contrast and tube voltage arises from the energy-dependent nature of X-ray interactions: low-energy photons are dominated by photoelectric absorption, enabling greater energy deposition within the medium, whereas high-energy photons interact primarily through Compton scattering, resulting in reduced energy transfer and lower light output. At lower tube voltage (50kV), The X-ray spectrum is weighted toward lower photon energies where photoelectric absorption dominates. The tungsten target acts as an effective spectral filter, strongly attenuating low-energy photons through photoelectric interactions while transmitting only a reduced fraction of higher-energy photons. Consequently, the scintillator region beneath the tungsten receives both a reduced photon count and photons with higher average energy, resulting in less energy deposited per photon, which further weakens the scintillation output. In marked contrast, the uncovered region receives the full, unattenuated photon flux, enriched in low-energy photons that interact more efficiently with the scintillator, resulting in substantially greater emissions. This combined effect, both photon number and energy transfer efficiency, yields high radiographic contrast, with the tungsten-covered region appearing distinctly dark and the uncovered region appearing bright. However, the SNR in the attenuated region remains limited by the low total photon flux, constraining the signal quality despite excellent contrast.

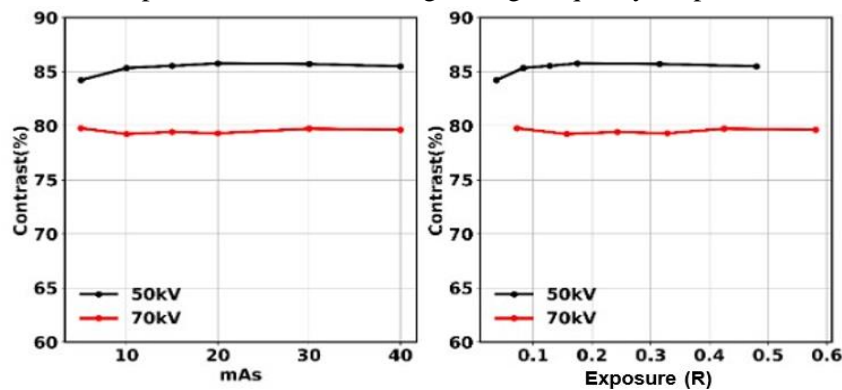


Figure 19. Investigation of relation between image’s contrast and tube’s voltage (kV) at various mAs, exposure dose.

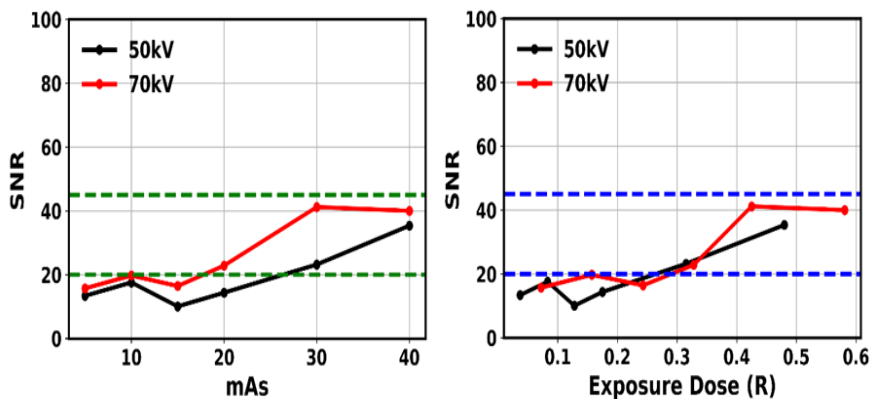


Figure 20. Investigation of dose efficiency in terms of Signal to Noise Ratio (SNR) versus mAs setting and measured dose at various kV.

At higher tube voltages (70 kV), the X-ray spectrum shifts toward higher photon energies, and Compton scattering becomes the dominant interaction mechanism. Compton-scattered and primary high-energy photons penetrate the tungsten target with substantially reduced attenuation due to the weak Z-dependence of Compton cross-section. However, because high-energy photons exhibit lower scintillation yield per photon, a consequence of reduced energy transfer to scintillator, the absolute light output from the attenuated region remains relatively dim despite increased photon transmission. Meanwhile, the uncovered region receives the full spectrum, now containing a greater ratio of higher-energy photons; although these contribute less to scintillation per photon, the total incident photon flux rises significantly with tube voltage. The net result is that radiographic contrast declines, not because the attenuated region becomes brighter (it remains dim), but because the uncovered region becomes even brighter, narrowing the brightness differential. Critically, by increasing tube voltage (kV), the total photon flux will be increased, then improves the signal-to-noise ratio. Thus, SNR and contrast move in opposite directions: SNR is improved at higher tube voltages while the contrast degraded, reflecting the competing energy-dependent responses of the X-ray spectrum and scintillator luminous yield. The signal-to-noise ratio (SNR) increases with X-ray tube voltage for a fixed exposure level (mAs), as illustrated in Fig. 20.

Overall, at the same exposure level (mAs) setting, higher tube voltages provide a larger photon flux and greater beam penetration, allowing more photons to reach the scintillator and contribute to image formation. This behavior reflects the fundamental trade-off in radiographic imaging: low tube voltages produce higher contrast due to efficient photoelectric absorption of low-energy photons, while high tube voltages enhance penetration and SNR through the predominance of high-energy, Compton-scattered photons. Representative X-ray images of the tungsten target and an electronic component, demonstrating the system's imaging performance across different exposure and voltage settings is illustrated in Fig. 21. Moreover, to demonstrate the modularity of the developed device, preliminary X-ray images were acquired using alternative commercial scintillators: LYSO:Ce and GAGG:Ce. Fig. 22 presents representative X-ray images of the tungsten target recorded with each scintillator at identical acquisition settings (70 kV-40 mAs). Clear images and visible fine structures confirm that the platform readily accommodates different scintillation screens without modification, validating the modular design approach.

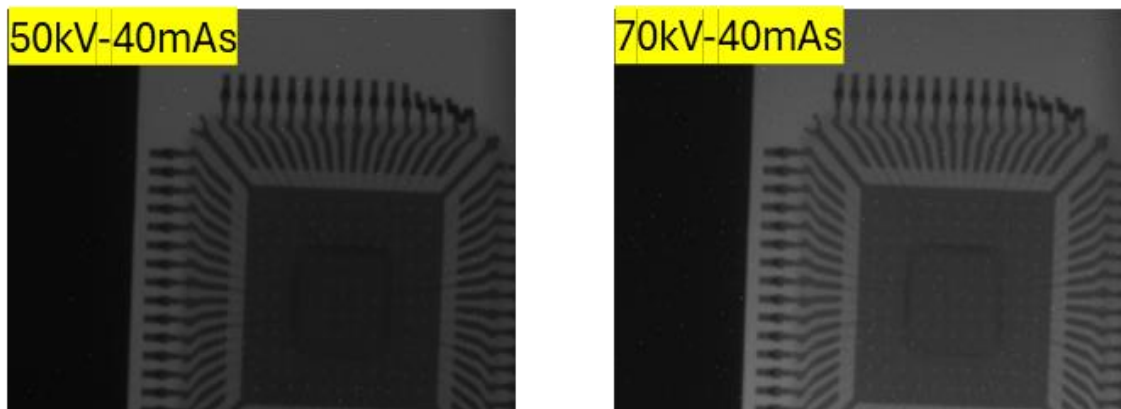


Figure 21. The recorded images of W target (dark area) alongside an electronic chip at X-ray of 50 and 70 kV, with a constant exposure level (tube current of 200 mA, and an exposure time of 200 ms).

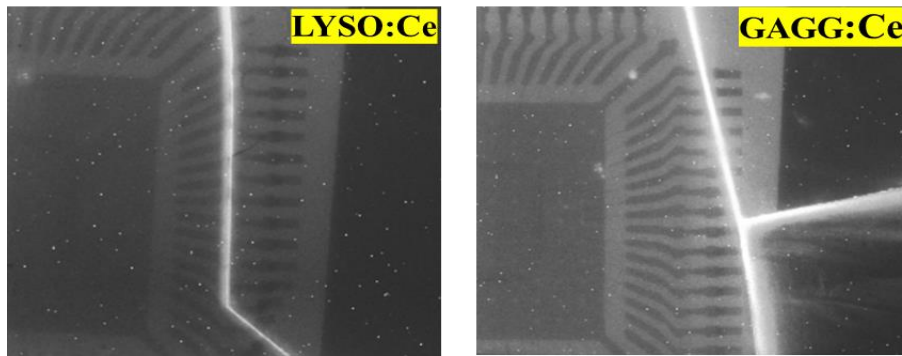


Figure 22. X-ray images of a tungsten (W) target positioned adjacent to an electronic chip, acquired using LYSO:Ce and GAGG:Ce scintillation screens under 70 kV - 40 mAs irradiation conditions. For enhanced visualization, the display range was adjusted to 0 - 1500 instead of the full 0-4095 range. The bright linear features observed in the images originate from cracks of the scintillation screens.

4. Conclusion

This study reports the development and characterization of a compact and cost-efficient X-ray imaging system based on a Raspberry Pi computer, its high efficiency, low noise camera module, a custom optical assembly, and a GOS scintillator, with a total material cost of approximately \$570. Systematic evaluation demonstrated spatial resolutions in the range of approximately 68 and 25 lp/mm (MTF_{20}) under ambient light and various X-ray exposure conditions. Optimization of camera parameters and exposure settings enabled effective enhancement of image contrast, signal-to-noise ratio, and spatial resolution, reaffirming fundamental radiographic principles within an accessible hardware framework.

The validated system exhibits strong technical feasibility for high-resolution digital radiography at substantially reduced cost. Its modular architecture allows flexible adaptation for diverse purposes, including instructional demonstrations of imaging physics, low-cost industrial non-destructive testing, and laboratory-scale research. Furthermore, owing to its indirect conversion configuration, the developed device is inherently versatile and, with an appropriate choice of scintillation screen, can be adapted for radiography applications with various excitation beams. This versatility extends its applicability to a broad range of scientific and industrial domains, such as non-destructive evaluation, materials characterization, and nuclear diagnostics. Although DQE and NNPS studies were not conducted, comprehensive characterization of resolution, contrast, and noise confirms the robustness of the imaging performance. Overall, the proposed platform provides a practical and accessible pathway toward high-resolution digital radiography and related modalities, promoting broader adoption of imaging technologies in scientific, educational, and field deployable contexts.

Acknowledgments

These investigations were supported by the National Research Foundation of Korea (NRF), funded by the Ministry of Science and Technology, Korea (MEST) (No. RS-2018-NR031074 and RS-2024-00348317). This project is partly funded by National Research Council of Thailand (NRCT) (Grant No. N42A680125). We are also grateful to Thailand Science Research and

Innovation and Nakhon Pathom Rajabhat University for supporting this research. This research was supported by Fundamental Fund (2026), Chiang Mai University. The authors would like to express their sincere appreciation to Dr. Jeongmin Park at the Korea Atomic Energy Institute for kindly providing the calibrated RadEye Remote HR system used in the initial validation experiments.

References

- [1] W. C. Röntgen, “*On a New Kind of Rays*,” *Science* **3**, (1896) 227.
- [2] J. H. Scatliff and P. J. Morris, “*From Röntgen to Magnetic Resonance Imaging*,” *North Carolina Medical Journal* **75**, (2014) 111.
- [3] G. Zentai, *X-Ray Imaging for Homeland Security*, in 2008 IEEE International Workshop on Imaging Systems and Techniques, IEEE, (2008).
- [4] G. Chen, “*Understanding X-ray cargo imaging*,” *Nuclear Instruments and Methods in Physics Research Section B: Beam Interactions with Materials and Atoms* **241**, North-Holland, (2005) 810.
- [5] J. HOWELL, “*EARLY CLINICAL USE OF THE X-RAY*,” *Transactions of the American Clinical and Climatological Association* **127**, (2016) 341.
- [6] A. Arodzero, V. Alreja, S. Boucher, P. Burstein, P. Kulinich, R. C. Lanza, V. Palermo and M. Tran, *X-Ray Backscatter Security Inspection with Enhanced Depth of Effective Detection and Material Discrimination*, in 2021 IEEE Nuclear Science Symposium and Medical Imaging Conference (NSS/MIC), IEEE, (2021).
- [7] I. Uroukov and R. Speller, “*A Preliminary Approach to Intelligent X-ray Imaging for Baggage Inspection at Airports*,” *Signal Processing Research* **4**, (2015) 1.
- [8] S. U. Khan, I. U. Khan, I. Ullah, N. Saif and I. Ullah, “*A review of airport dual energy X-ray baggage inspection techniques: Image enhancement and noise reduction*,” *Journal of X-Ray Science and Technology: Clinical Applications of Diagnosis and Therapeutics* **28**, (2020) 481.
- [9] O. E. Wetter, “*Imaging in airport security: Past, present, future, and the link to forensic and clinical radiology*,” *Journal of Forensic Radiology and Imaging* **1**, Elsevier, (2013) 152.
- [10] D. Mery, D. Saavedra and M. Prasad, “*X-Ray Baggage Inspection With Computer Vision: A Survey*,” *IEEE Access* **8**, (2020) 145620.
- [11] M. Holler, M. Guizar-Sicairos, E. H. R. Tsai, R. Dinapoli, E. Müller, O. Bunk, J. Raabe and G. Aepli, “*High-resolution non-destructive three-dimensional imaging of integrated circuits*,” *Nature* **543**, (2017) 402.
- [12] G. Chen, “*Understanding X-ray cargo imaging*,” *Nuclear Instruments and Methods in Physics Research Section B: Beam Interactions with Materials and Atoms* **241**, North-Holland, (2005) 810.
- [13] K. Wells and D. A. Bradley, “*A review of X-ray explosives detection techniques for checked baggage*,” *Applied Radiation and Isotopes* **70**, Pergamon, (2012) 1729.
- [14] T. W. Rogers, N. Jaccard, E. J. Morton and L. D. Griffin, “*Automated X-ray image analysis for cargo security: Critical review and future promise*,” *Journal of X-Ray Science and Technology* **25**, IOS Press, (2017) 33.
- [15] N. Jaccard, T. W. Rogers, E. J. Morton and L. D. Griffin, “*Detection of concealed cars in complex cargo X-ray imagery using Deep Learning*,” *Journal of X-Ray Science and Technology* **25**, IOS Press, (2017) 323.
- [16] D. Anderson and D. Vukadinovic, *X-Ray Baggage Screening and Artificial Intelligence (AI) A Technical Review of Machine Learning Techniques for X-Ray Baggage Screening*, in JRC Science for Policy Report, (2022).
- [17] R. Rakay and M. Vagas, *The Comparison of Machine Vision Approaches for Standard Industrial Solutions*, in 2024 25th International Carpathian Control Conference (ICCC), IEEE, (2024).
- [18] C. Amadou, G. Bera, M. Ezziiane, L. Chami, T. Delbot, A. Rouxel, M. Leban, G. Herve, F. Menegaux, et al., “*18F-Fluorocholine PET/CT and Parathyroid 4D Computed Tomography for*

- Primary Hyperparathyroidism: The Challenge of Reoperative Patients,*” World Journal of Surgery **43**, (2019) 1232.
- [19] M. S. Hofman, N. Lawrentschuk, R. J. Francis, C. Tang, I. Vela, P. Thomas, N. Rutherford, J. M. Martin, M. Frydenberg, et al., “*Prostate-specific membrane antigen PET-CT in patients with high-risk prostate cancer before curative-intent surgery or radiotherapy (proPSMA): a prospective, randomised, multicentre study,*” The Lancet **395**, (2020) 1208.
- [20] Y. Jin, D. Ni, L. Gao, X. Meng, Y. Lv, F. Han, H. Zhang, Y. Liu, Z. Yao, et al., “*Harness the Power of Upconversion Nanoparticles for Spectral Computed Tomography Diagnosis of Osteosarcoma,*” Advanced Functional Materials **28**, (2018).
- [21] W. J. H. Veldkamp, L. J. M. Kroft, M. V. Boot, B. J. A. Mertens and J. Geleijns, “*Contrast-detail evaluation and dose assessment of eight digital chest radiography systems in clinical practice,*” European Radiology **16**, Eur Radiol, (2006) 333.
- [22] T. Martin, A. Koch and M. Nikl, “*Scintillator materials for x-ray detectors and beam monitors,*” MRS Bulletin **42**, (2017) 451.
- [23] J. H. Heo, D. H. Shin, J. K. Park, D. H. Kim, S. J. Lee and S. H. Im, “*High-Performance Next-Generation Perovskite Nanocrystal Scintillator for Nondestructive X-Ray Imaging,*” Advanced Materials **30**, (2018).
- [24] A. Koch, “*Lens coupled scintillating screen-CCD X-ray area detector with a high detective quantum efficiency,*” Nuclear Instruments and Methods in Physics Research Section A: Accelerators, Spectrometers, Detectors and Associated Equipment **348**, North-Holland, (1994) 654.
- [25] J. Yorkston, “*Recent developments in digital radiography detectors,*” Nuclear Instruments and Methods in Physics Research Section A: Accelerators, Spectrometers, Detectors and Associated Equipment **580**, North-Holland, (2007) 974.
- [26] T. Martin and A. Koch, “*Recent developments in X-ray imaging with micrometer spatial resolution,*” Journal of Synchrotron Radiation **13**, (2006) 180.
- [27] B. J. Kim, G. Cho, B. Kyung Cha and B. Kang, “*An X-ray imaging detector based on pixel structured scintillator,*” Radiation Measurements **42**, Pergamon, (2007) 1415.
- [28] D. Linardatos, G. Fountos, I. Valais and C. Michail, “*A Novel Method for Developing Thin Resin Scintillator Screens and Application in an X-ray CMOS Imaging Sensor,*” Sensors 2023, Vol. 23, Page 6588 **23**, Multidisciplinary Digital Publishing Institute, (2023) 6588.
- [29] M. J. Yaffe and J. A. Rowlands, “*X-ray detectors for digital radiography,*” Physics in Medicine and Biology **42**, Institute of Physics Publishing, (1997) 1.
- [30] M. Körner, C. H. Weber, S. Wirth, K. J. Pfeifer, M. F. Reiser and M. Treitl, “*Advances in digital radiography: Physical principles and system overview,*” Radiographics **27**, Radiographics, (2007) 675.
- [31] E. S.-I. T. on N. Science and undefined 1987, “*Recent measurements on scintillator-photodetector systems,*” ieeexplore.ieee.org SakaiIEEE Transactions on Nuclear Science, 1987•ieeexplore.ieee.org.
- [32] L. Lu, M. Sun, Q. Lu, T. Wu and B. Huang, “*High energy X-ray radiation sensitive scintillating materials for medical imaging, cancer diagnosis and therapy,*” Nano Energy **79**, Elsevier, (2021) 105437.
- [33] C. Michail, I. Valais, I. Seferis, N. Kalyvas, G. Fountos and I. Kandarakis, “*Experimental measurement of a high resolution CMOS detector coupled to CsI scintillators under X-ray radiation,*” Radiation Measurements **74**, Pergamon, (2015) 39.
- [34] R. H. Harrison, “*Digital radiography — a review of detector design,*” Nuclear Instruments and Methods in Physics Research Section A: Accelerators, Spectrometers, Detectors and Associated Equipment **310**, North-Holland, (1991) 24.
- [35] M. V. Prummel, D. Muradali, R. Shumak, V. Majpruz, P. Brown, H. Jiang, S. J. Done, M. J. Yaffe and A. M. Chiarelli, “*Digital compared with screen-film mammography: Measures of diagnostic*

- accuracy among women screened in the Ontario breast screening program,” *Radiology* **278**, Radiological Society of North America Inc., (2016) 365.
- [36] R. G. Swee, J. E. Gray, J. W. Beabout, R. A. McLeod, K. L. Cooper, J. R. Bond and D. E. Wenger, “Screen-film versus computed radiography imaging of the hand: A direct comparison,” *American Journal of Roentgenology* **168**, American Roentgen Ray Society, (1997) 539.
- [37] A. G. Haus and J. E. Cullinan, “Screen film processing systems for medical radiography: a historical review,” *Radiographics: a review publication of the Radiological Society of North America, Inc* **9**, Radiographics, (1989) 1203.
- [38] A. Engidayehu and O. Sahu, “Enzymatic recovery of silver from waste radiographic film: Optimize with response surface methodology,” *Sustainable Chemistry and Pharmacy* **15**, (2020) 100224.
- [39] K. Konstantinidou, S. Strekopytov, E. Humphreys-Williams and M. Kearney, “Identification of cellulose nitrate X-ray film for the purpose of conservation: Organic elemental analysis,” *Studies in Conservation* **62**, (2017) 24.
- [40] X. Ou, X. Chen, X. Xu, L. Xie, X. Chen, Z. Hong, H. Bai, X. Liu, Q. Chen, et al., “Recent Development in X-Ray Imaging Technology: Future and Challenges,” *Research* **2021**, (2021).
- [41] P. Leblans, D. Vandenbroucke and P. Willems, “Storage phosphors for medical imaging,” *Materials* **4**, Materials (Basel), (2011) 1034.
- [42] A. R. Cowen, A. G. Davies and S. M. Kengyelics, “Advances in computed radiography systems and their physical imaging characteristics,” *Clinical Radiology* **62**, (2007) 1132.
- [43] J. A. Rowlands, “The physics of computed radiography,” *Physics in Medicine and Biology* **47**, (2002) R123.
- [44] H. Huang and S. Abbaszadeh, “Recent Developments of Amorphous Selenium-Based X-Ray Detectors: A Review,” *IEEE Sensors Journal* **20**, (2020) 1694.
- [45] E. Kotter and M. Langer, “Digital radiography with large-area flat-panel detectors,” *European Radiology* **12**, (2002) 2562.
- [46] A. R. Cowen, S. M. Kengyelics and A. G. Davies, “Solid-state, flat-panel, digital radiography detectors and their physical imaging characteristics,” *Clinical Radiology* **63**, (2008) 487.
- [47] H. G. Chotas and C. E. Ravin, “Digital Chest Radiography with a Solid-state Flat-Panel X-ray Detector: Contrast-Detail Evaluation with Processed Images Printed on Film Hard Copy,” *Radiology* **218**, (2001) 679.
- [48] M. Spahn, “Flat detectors and their clinical applications,” *European Radiology* **15**, (2005) 1934.
- [49] U. Neitzel, “Status and prospects of digital detector technology for CR and DR,” *Radiation Protection Dosimetry* **114**, (2005) 32.
- [50] A. C. Konstantinidis, M. B. Szafraniec, R. D. Speller and A. Olivo, “The DEXELA 2923 CMOS X-ray detector: A flat panel detector based on CMOS active pixel sensors for medical imaging applications,” *Nuclear Instruments and Methods in Physics Research Section A: Accelerators, Spectrometers, Detectors and Associated Equipment* **689**, North-Holland, (2012) 12.
- [51] A. R. Cowen, S. M. Kengyelics and A. G. Davies, “Solid-state, flat-panel, digital radiography detectors and their physical imaging characteristics,” *Clinical Radiology* **63**, (2008) 487.
- [52] M. J. Yaffe and J. A. Rowlands, “X-ray detectors for digital radiography,” *Physics in Medicine and Biology* **42**, (1997) 1.
- [53] X. Badel, B. Norlin, P. Kleimann, L. Williams, S. J. Moody, G. C. Tyrrell, C. Frojdh and J. Linnros, “Performance of scintillating waveguides for CCD-based X-ray detectors,” *IEEE Transactions on Nuclear Science* **53**, (2006) 3.
- [54] E. Samei and M. J. Flynn, “An experimental comparison of detector performance for direct and indirect digital radiography systems,” *Medical Physics* **30**, John Wiley and Sons Ltd, (2003) 608.
- [55] J. A. Seibert, “Digital radiography: Image quality and radiation dose,” *Health Physics* **95**, (2008) 586.
- [56] G. Andria, F. Attivissimo, G. Guglielmi, A. M. L. Lanzolla, A. Maiorana and M. Mangiantini, “Towards patient dose optimization in digital radiography,” *Measurement* **79**, Elsevier, (2016) 331.

- [57] G. J. Bansal, “*Digital radiography. A comparison with modern conventional imaging,*” *Postgraduate Medical Journal* **82**, (2006) 425.
- [58] H. K. Kim, J. K. Ahn and G. Cho, “*Development of a lens-coupled CMOS detector for an X-ray inspection system,*” *Nuclear Instruments and Methods in Physics Research Section A: Accelerators, Spectrometers, Detectors and Associated Equipment* **545**, North-Holland, (2005) 210.
- [59] J. A. Seibert, “*Tradeoffs between image quality and dose,*” *Pediatric Radiology* **34**, (2004) S183.
- [60] C. M. Ardila, A. M. Vivares-Builes and E. Pineda-Vélez, “*Image Quality, Radiation Dose, and Patient Comfort Associated with Wireless Sensors in Digital Radiography: A Systematic Review.,*” *Dentistry journal* **12**, Multidisciplinary Digital Publishing Institute (MDPI), (2024).
- [61] B.-J. Kim, G. Cho, B. Kyung Cha and B. Kang, “*An X-ray imaging detector based on pixel structured scintillator,*” *Radiation Measurements* **42**, (2007) 1415.
- [62] B. K. Cha, J. Y. Kim, T. J. Kim, C. Sim and G. Cho, “*Fabrication and imaging characterization of high sensitive CsI(Tl) and Gd₂O₂S(Tb) scintillator screens for X-ray imaging detectors,*” *Radiation Measurements* **45**, Pergamon, (2010) 742.
- [63] C. W. Jeong, S. C. Joo, J. H. Ryu, J. Lee, K. W. Kim and K. H. Yoon, “*Development of a Mini-Mobile Digital Radiography System by Using Wireless Smart Devices,*” *Journal of Digital Imaging* **27**, Springer New York LLC, (2014) 443.
- [64] P. Magnan, “*Detection of visible photons in CCD and CMOS: A comparative view,*” *Nuclear Instruments and Methods in Physics Research Section A: Accelerators, Spectrometers, Detectors and Associated Equipment* **504**, North-Holland, (2003) 199.
- [65] E. R. Fossum, “*CMOS image sensors: electronic camera-on-a-chip,*” *IEEE Transactions on Electron Devices* **44**, (1997) 1689.
- [66] I. A. Elbakri, B. J. McIntosh and D. W. Rickey, “*Physical characterization and performance comparison of active- and passive-pixel CMOS detectors for mammography,*” *Physics in Medicine and Biology* **54**, (2009) 1743.
- [67] P. Allé, E. Wenger, S. Dahaoui, D. Schaniél and C. Lecomte, “*Comparison of CCD, CMOS and Hybrid Pixel x-ray detectors: detection principle and data quality,*” *Physica Scripta* **91**, IOP Publishing, (2016) 063001.
- [68] “*Raspberry Pi 4 Model B – Raspberry Pi*”<https://www.raspberrypi.com/products/raspberry-pi-4-model-b/> (2 July 2025).
- [69] “*Raspberry Pi High Quality Camera – Raspberry Pi*”<https://www.raspberrypi.com/products/raspberry-pi-high-quality-camera/> (2 July 2025).
- [70] Huu-Quoc Nguyen, Ton Thi Kim Loan, Bui Dinh Mao and Eui-Nam Huh, *Low Cost Real-Time System Monitoring Using Raspberry Pi*, in 2015 Seventh International Conference on Ubiquitous and Future Networks, IEEE, (2015).
- [71] A. D. Deshmukh and U. B. Shinde, *A Low Cost Environment Monitoring System Using Raspberry Pi and Arduino with Zigbee*, in 2016 International Conference on Inventive Computation Technologies (ICICT), IEEE, (2016).
- [72] H. Maulana and Al-Khowarizmi, “*Analyze and Designing Low-Cost Network Monitoring System Using Icinga and Raspberry Pi,*” *IOP Conference Series: Earth and Environmental Science* **704**, (2021) 012038.
- [73] M. Wang, K. Y. Koo, C. Liu and F. Xu, “*Development of a low-cost vision-based real-time displacement system using Raspberry Pi,*” *Engineering Structures* **278**, Elsevier, (2023) 115493.
- [74] SONY, *Product Information: IMX477-AACK Diagonal 7.857 Mm (Type 1/2.3) 12.3 Mega-Pixel CMOS Image Sensor with Square Pixel for Color Cameras*, (2018).
- [75] A. M. Botti, L. Barreiro, S. Benas, C. Bonifazi, F. Cammarata, M. Danussi, E. Depaoli, P. López Maggi, J. Pérez Lanzillotta, et al., *Low-Cost CMOS Tech for Inclusive High-Energy Physics Education*, in Proceedings of 39th International Cosmic Ray Conference — PoS(ICRC2025), Sissa Medialab, Trieste, Italy, (2025).

- [76] M. Estriebeau and P. Magnan, “Fast MTF measurement of CMOS imagers using ISO 12333 slanted-edge methodology,” <https://doi.org/10.1117/12.513320> **5251**, SPIE, (2004) 243.
- [77] R. A. Sones and G. T. Barnes, “A method to measure the MTF of digital x ray systems,” *Medical Physics* **11**, (1984) 166.
- [78] E. Samei, M. J. Flynn and D. A. Reimann, “A method for measuring the presampled MTF of digital radiographic systems using an edge test device,” *Medical Physics* **25**, (1998) 102.
- [79] Ehsan Samei, *Performance of Digital Radiographic Detectors: Quantification and Assessment Methods 1*, (2003).
- [80] K. Masaoka, T. Yamashita, Y. Nishida and M. Sugawara, “Modified slanted-edge method and multidirectional modulation transfer function estimation,” *Optics Express* **22**, (2014) 6040.
- [81] I. E. Commission, “Medical electrical equipment-Characteristics of digital X-ray imaging devices-Part 1-1: Determination of the Detective Quantum Efficiency-Detectors used in radiographic imaging,” IEC 62220-1-1, International Electrotechnical Commission, (2015).
- [82] I.-I. E. Commission, “Medical Electrical Equipment–Charac-teristics of Digital X-Ray Imaging Devices–Part 1: Determination of the Detective Quantum Efficiency, IEC 62220-1,” Geneva, Switzerland, (2003).
- [83] K. Rossmann, “Point spread-function, line spread-function, and modulation transfer function. Tools for the study of imaging systems.,” *Radiology* **93**, (1969) 257.
- [84] J. Dobbins, *Image Quality Metrics for Digital Systems*, in Handbook of Medical Imaging, Volume 1. Physics and Psychophysics, SPIE, 1000 20th Street, Bellingham, WA 98227-0010 USA.
- [85] “Remote RadEye HR | Teledyne Vision Solutions”<https://www.teledynevisionsolutions.com/products/remote-radeye-hr/?model=RM1426&vertical=tv%20-%20dalsa%20-%20oem&segment=tv%20-%20dalsa%20-%20oem> (2 July 2025).
- [86] “MIN-R Screens - Image Capture - Carestream Health, Inc.”<https://www.carestream.com/nl/be/medical/products/womenshealthcare/film-solutions-for-mammography/screens-and-cassettes-for-mammography/min-r-screens> (3 July 2025).
- [87] “Documentation & Technical Drawings | Teledyne Vision Solutions”<https://www.teledynevisionsolutions.com/support/support-center/documentation/?q=Remote+RadEye&page=1> (17 September 2025).
- [88] L. J. M. Kroft, W. J. H. Veldkamp, B. J. A. Mertens, M. V. Boot and J. Geleijns, “Comparison of eight different digital chest radiography systems: Variation in detection of simulated chest disease,” *American Journal of Roentgenology* **185**, American Roentgen Ray Society, (2005) 339.
- [89] H. G. Chotas, J. T. Dobbins and C. E. Ravin, “Principles of digital radiography with large-area, electronically readable detectors: A review of the basics,” *Radiology* **210**, Radiological Society of North America Inc., (1999) 595.
- [90] M. K. Cho, H. K. Kim, T. Graeve, S. M. Yun, C. H. Lim, H. Cho and J. M. Kim, “Measurements of X-ray imaging performance of granular phosphors with direct-coupled CMOS sensors,” *IEEE Transactions on Nuclear Science* **55**, (2008) 1338.
- [91] E. R. Fossum, “CMOS active pixel image sensors,” *Nuclear Instruments and Methods in Physics Research Section A: Accelerators, Spectrometers, Detectors and Associated Equipment* **395**, North-Holland, (1997) 291.
- [92] Philip Willmott, *The Interaction of X-rays with Matter*, in An Introduction to Synchrotron Radiation, Wiley, (2019).
- [93] Jens Als-Nielsen and Des McMorrow, *X-rays and Their Interaction with Matter*, in Elements of Modern X-ray Physics, Wiley, (2011).
- [94] G. Poludniowski, A. Omar, R. Bujila and P. Andreo, “Technical Note: SpekPy v2.0—a software toolkit for modeling x-ray tube spectra,” *Medical Physics* **48**, John Wiley and Sons Ltd, (2021) 3630.

- [95] R. Vorbau and G. Poludniowski, “*Technical note: SpekPy Web—online x-ray spectrum calculations using an interface to the SpekPy toolkit*,” *Journal of Applied Clinical Medical Physics* **25**, John Wiley and Sons Ltd, (2024).